

Original Article

Development of Less Computational Costly Ultrasound Imaging Using the Finite Element Method

Ahamed- Al- Arifin¹, S.M. Baque Billah², Kazi Muhammad Asif Ashrafi³

^{1, 2, 3}Department of EEE, East Delta University, Chattogram, Bangladesh.

¹Corresponding Author: ahamed.a@eastdelta.edu.bd

Received: 23 December 2023

Revised: 02 April 2024

Accepted: 09 April 2024

Published: 26 May 2024

Abstract - Elastography or strain imaging using ultrasound has been found to be useful for determining malignant tissue via state-of-the-art medical imaging. The strain is subjected to tissue displacement measurements. Most of the algorithms that are used to find tissue displacement via elastography are one-dimensional and direct strain imaging techniques are also computationally costly. To overcome these problems, this paper introduces a 2-D cross-correlation algorithm to compute the time delay in two directions and the workflow of the strain imaging has been modified to reduce the computation cost of imaging. The MATLAB tic toc function is used to determine the simulation time of each step of the modified workflow. To accomplish this work, a synthetic two-dimensional tissue-mimicking phantom was made by using the finite element-based software ANSYS. To obtain the radio frequency (RF) signal, different simulations were performed in the ultrasound simulation software FIELD II. The cross-correlation coefficient obtained from the ultrasound simulation was mapped using the MATLAB surf tool. The attained map shows an auspicious result in differentiating between benign and malignant tissue. Additionally, the proposed algorithm has a lower computational cost in terms of simulation time, with a value of 222.072322 seconds, in contrast with the simulation time of conventional strain imaging, which has a value of more than 222.093015 seconds. Therefore, by applying the above imaging algorithm and procedure to a real-world 3-D scenario, we may develop a more sophisticated imaging technique that is less computationally costly.

Keywords - Ultrasound, Elastography, FEM, 2D cross-correlation, Surf tool.

1. Introduction

Measuring the time delay of ultrasound echo signals has been a mainstay for a vast span of ultrasound-based signal processing employments. It is part and parcel of blood flow estimation, tissue elasticity measurement or elastography [1-4], tissue velocity estimation [5-8], etc. In time-delay estimation, the estimators assess the delay between the reflected signals to the transducer. The measured delay could be phase-shift or time-shift between successions of echo signals [7]. Based on the domain, the estimator is operated, and the signal delay estimator can be classified into different classes [9-12]. The time-shift estimator of these estimators is extensively used in tissue motion estimation. This estimator identifies the minimum or maximum of a pattern-matching algorithm. The signal in a certain window of the base signal is fixed to be a pattern, and an algorithm is utilized to match the pattern in the delayed signal. Various pattern-matching algorithms are used in these time-delay estimations [9,13,14].

Currently, elastography has been a very popular imaging technique for the past two decades. One of the works for elastography is to estimate the delay among two RF signals (ante and post-compressed tissue). The estimated

displacement is basically a function of time. Therefore, the measured displacement is basically the time delay. Many authors have used different algorithms to determine the delay before and after RF signal compression. The most conventional algorithm is the time-domain cross-correlation approach [1].

The largest value achieved from the cross-correlation technique of the ante- and post-compression RF signals gives us the displacements for the Case of the time domain cross-correlation method. Other methods, like the Sum Absolute Difference (SAD), normalized cross-correlation, and Sum Squared Difference (SSD) methods etc., are utilized to find the time delay [9]. The normalized cross-correlation finds the matching point between signals by looking for the location of the highest value in the image matrices [15].

In the sum of the absolute difference method, a small region (window) is chosen for imaging. For each window of the image, the best matching of the chosen window is searched. A thick map of disparity could be generated by overlapping the chosen window with the window of the searched area [16]. The sum of the squared differences



window-to-window measurement occurs. The window difference between two images is multiplied, and the result is squared.

After squaring, the summation of squares is calculated. The position of the lowest value of the image matrices gives us the matching point [17]. In this research, 2D cross-correlation is utilized to evaluate the delay among two signals. 2D cross-correlation is the 2D version of general cross-correlation and is used to match two different signals as a function of the delay in relation to another [18].

The abovementioned methods are based on the window-based delay estimation technique. In those methods the average time shift is calculated for the samples that are contained in the window. The window size and the amount of lapping among windows affect this estimator's performance [19].

The problem regarding the execution of the estimators increases when the time-delay estimator uses multiple window sizes [20,21]. To improve the performance of the estimator, the sample tracking algorithm is a better delay estimation algorithm than windowing. This algorithm estimates each delayed pulse-echo signal sample's time shift in relation to the base signal [22].

Ultrasound imaging has been a very popular imaging technique in recent years. The main reason behind this could be the use of a noninvasive technique. Detecting abnormalities in human tissue biopsies has been used as a medical tool for many years. However, performing biopsies of the human body is painful and hazardous because a long and thick needle is used to collect the sample from the human body. This means that the technique is invasive. Therefore, to overcome this pain, a noninvasive ultrasound imaging technique named elastography was first introduced by J. Ophir in his paper [1]. After its introduction, elastography was developed by many authors in different ways.

In elastography, tissue imaging is basically based on the elastic properties of the tissue. Different elastic properties such as strain, stress, and Young's modulus are involved in this imaging. Elastography is typically the estimation of the strain of a given tissue under a particular stress applied to the tissue. First, the ultrasound echoes are gathered before and after the tissue is perturbed to a slight exterior force on the top using an ultrasound transducer [23].

The acquired ultrasound signal is normally a time-domain signal. Then, the strain is estimated using different algorithms from the ante- and post-compression ultrasound echo signals. These algorithms can be graded into two groups:

- gradient-based estimation [1,24-28] and
- direct strain estimation [29-32].

The signal acquired from the ante- and post-compression data is basically a time-delay signal. As discussed in the literature review, the algorithms that are used in time-delay estimation are pattern-matching algorithms. The signals taken from pre- and post-compressed tissue are broken down into windows. In each window, there are several echo signals. The pre-compression signal acts as a reference signal and an algorithm is used to match the pattern in the post-compression signal [9, 13, 14]. Most pattern-matching algorithms involve 1-D algorithms, which measure the displacement of any signal only in the axial direction [1, 23, 24, 33]. In this paper, a 2-D algorithm named 2-D cross-correlation is used in time-delay estimation, which could provide additional real imaging scenarios [34].

Moreover, the abovementioned methods discussed in the literature review are based on window-based techniques. In this technique, the average time shift is measured for the samples that are contained in the window. The performance of these windowing estimators decreases when multiple window sizes are used [20,21]. To improve the performance of these estimators, a sample tracking algorithm is used in this paper, where the delayed echo signal is calculated for each sample relative to the reference signal [22].

Computational cost is one of the major concerns regarding this kind of imaging. Therefore, to reduce the computational cost, this paper does address strain imaging; rather, it estimates the cross-correlation coefficient using 2-D cross-correlation and maps it using the MATLAB surf tool [35]. To substantiate this, the proposed method is better than conventional strain imaging, and the MATLAB tic toc function is used to find the elapsed time for each step for both methods were compared. The correlated map shows the auspicious ability to differentiate between benign and malignant tissue.

2. Materials and Methods

For the simulation, a homogeneous 2D tissue phantom was made utilizing the software package ANSYS (ANSYS Inc., Canonsburg), which worked using the Finite Element Model.

The dimensions of the phantom were a 20mm×20mm square with an inclusion having a diameter of 10mm, and it mimicked the malignant tissue. The phantom was set as an elastic, isotropic, and linear material. The malignant tissue is represented by the inclusion, whereas the square represents the benign tissue.

The densities of both benign and malignant tissues were taken as 1050 kg-m⁻³ and 1500 kg-m⁻³ independently. The benign and malignant tissue's Poisson's ratio was 0.495. The sketching and the phantom geometric model are shown below.

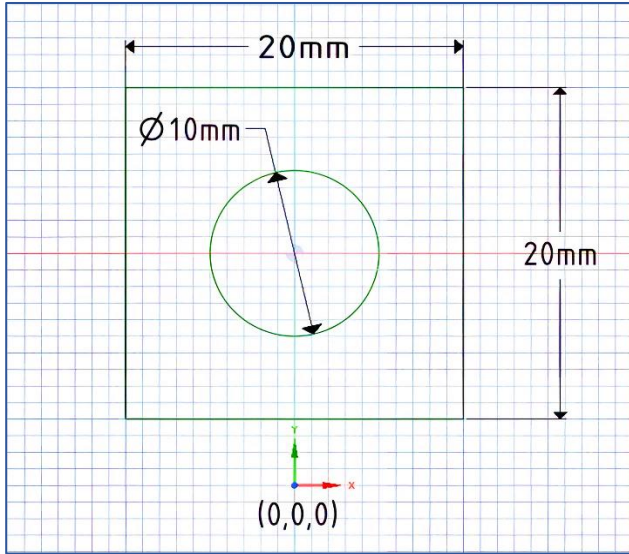


Fig. 1 2D sketching of the synthetic phantom

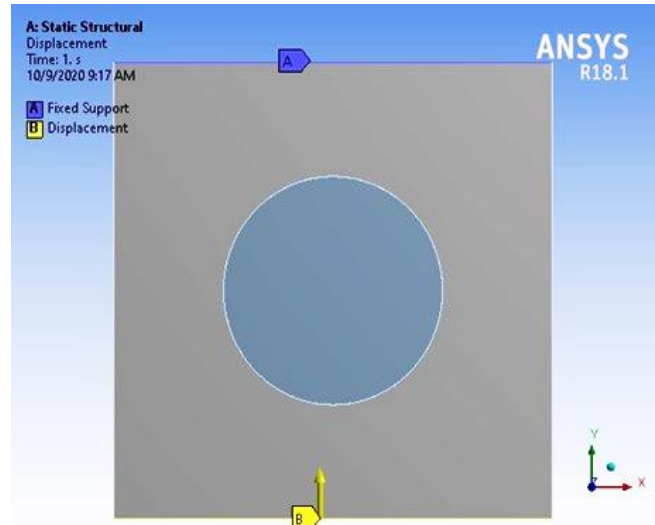


Fig. 4 Boundary conditions (displacement) for the synthetic model (for both 40 kPa and 80 kPa inclusions).

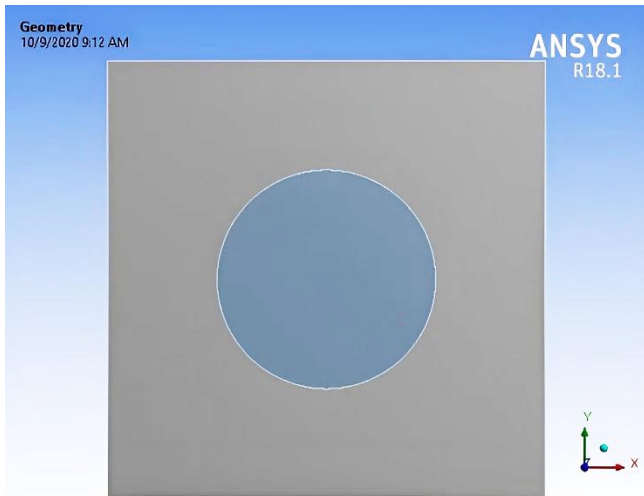


Fig. 2 Geometric model of the synthetic phantom

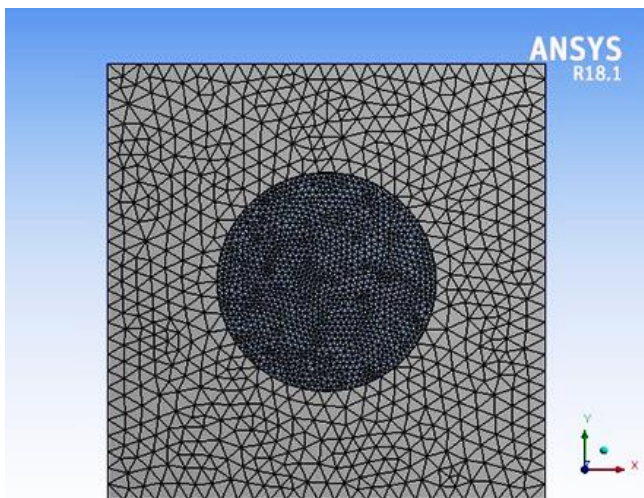


Fig. 3 Phantom's geometric model under meshing

2.1. Meshing of the Phantom Model

The model has meshed using the triangular method in the ANSYS design modeler. The total numbers of nodes and elements generated were 2049 and 3820 separately. The tumor is basically more compact than benign tissue, which is why the element size of malignant tissue (0.75 mm) was 3 times denser than that of benign tissue (0.25 mm). The meshing of the phantom is as follows:

2.2. Boundary Conditions for the Simulation

To accomplish the result, the top of the phantom was held fixed while the two left and right sides were allowed to move freely. A displacement boundary condition then moved the lower surface. The amount of displacement was set to 2% of the height of the phantom (0.4 mm). First, the model was simulated given boundary conditions when Young's moduli of the malignant and benign tissues were 40 kPa and 10 kPa, respectively. Then, the model was simulated with Young's moduli of 80 kPa and 10 kPa for the malignant and benign tissues, respectively. The model was also simulated for tissues with the same Young's Modulus (10 kPa) for both malignant and benign tissues.

2.3. Simulation of the Phantom

For a given applied displacement, the phantom was examined for both vertical and horizontal axes. The x-axis directional deformation can be achieved via horizontal axis simulation and directional deformation of the y-axis can be achieved via simulation along vertical direction. The x-axis deformation is acquired from the horizontal simulation. Similarly, the directional deformation of the y-axis is acquired from the vertical simulation. The model was also simulated for the total deformation of the phantom and the total strain experienced by the phantom. For later simulations, the displacement data for both axes can be obtained from the ANSYS design modeler platform.

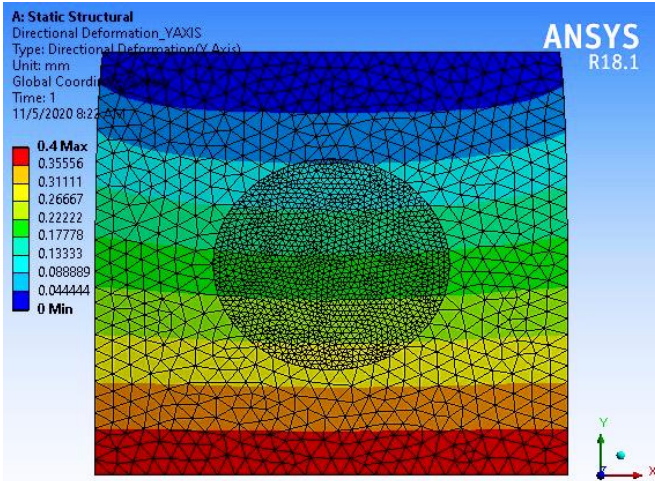


Fig. 5 Directional deformation (Y axis) for the same property containing inclusion as the background

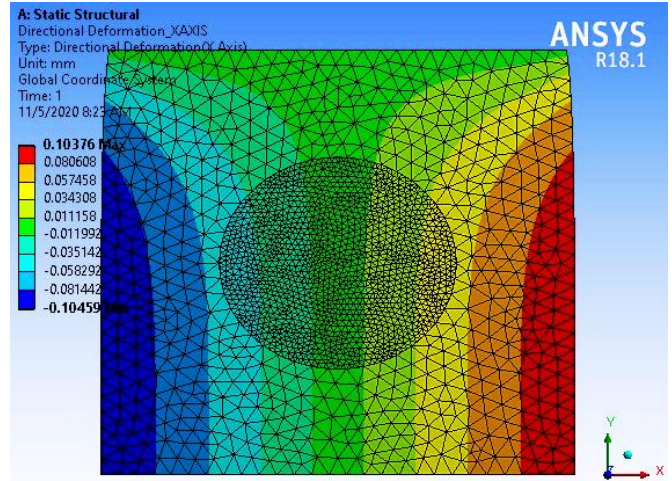


Fig. 8 Directional deformation (X-axis) for the same property containing the inclusion as the background

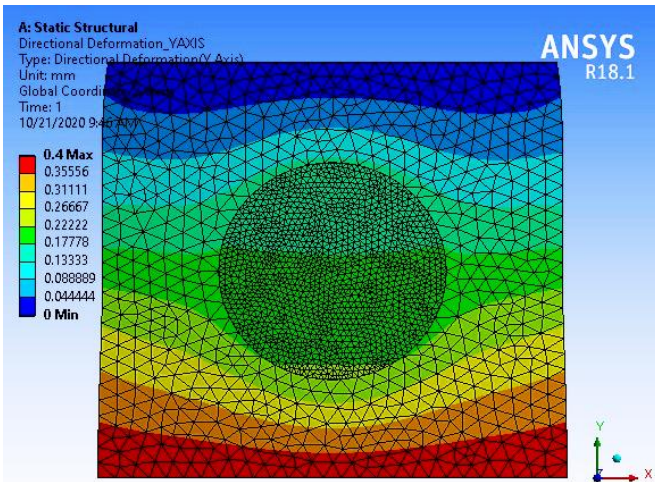


Fig. 6 Directional deformation (Y axis) for the 40 kPa inclusion

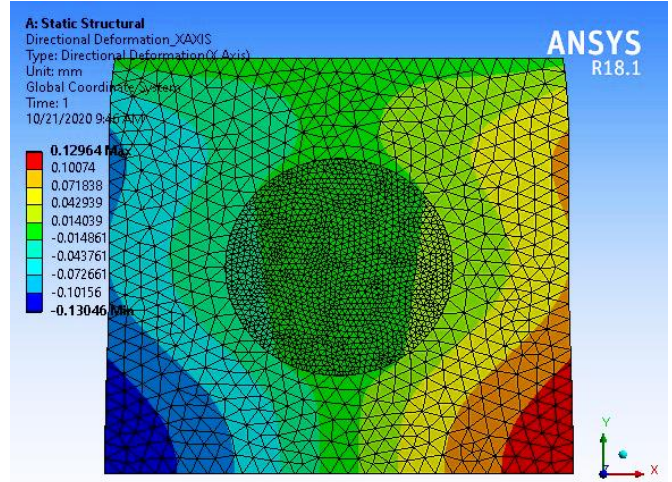


Fig. 9 Directional deformation (X-axis) for the 40 kPa inclusion

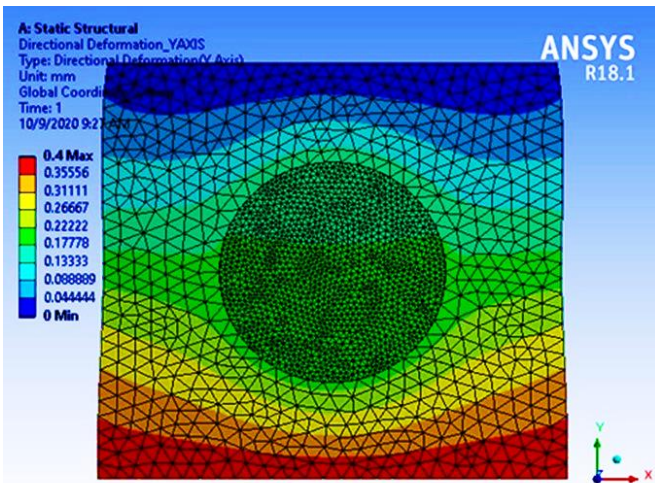


Fig. 7 Directional deformation (Y axis) for the 80 kPa inclusion

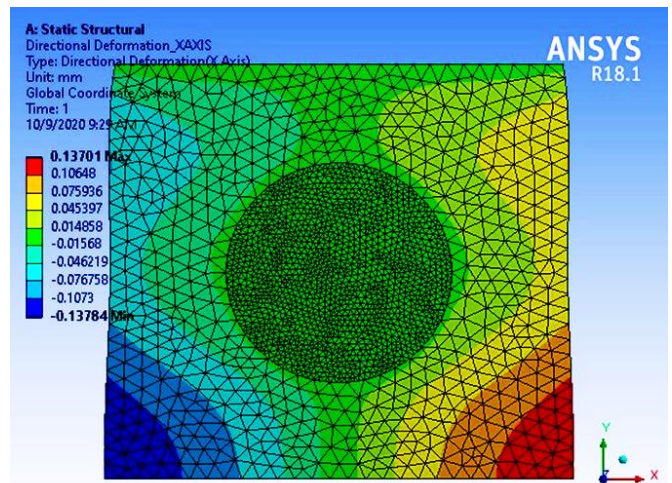


Fig. 10 Directional deformation (X-axis) for the 80 kPa inclusion

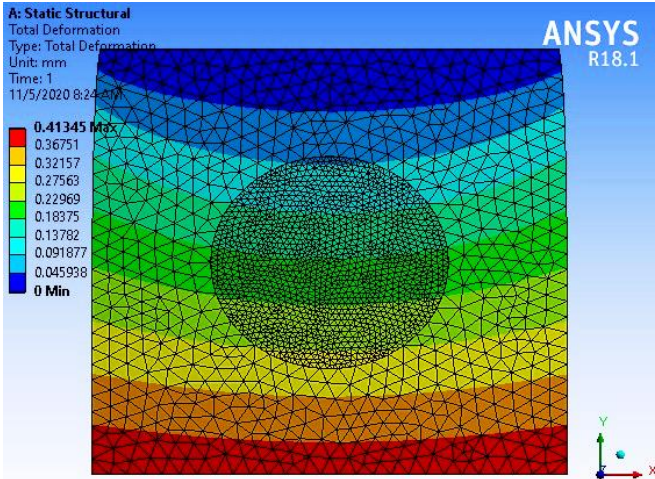


Fig. 11 Total deformation for the same property containing the inclusion as the background

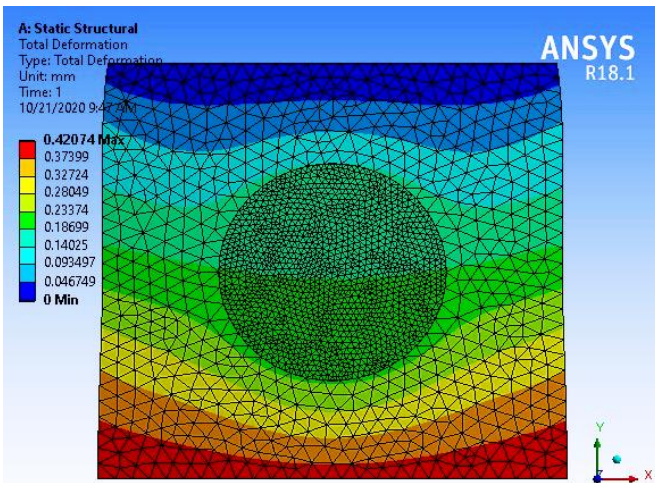


Fig. 12 Total deformation (X-axis) for the 40 kPa inclusion

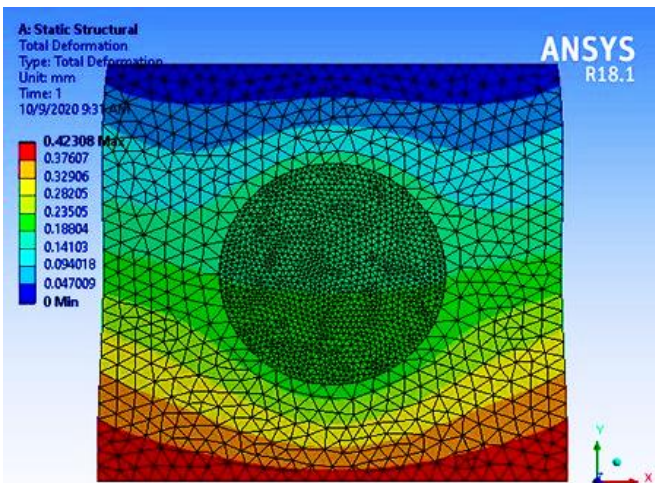


Fig. 13 Total deformation (X-axis) for the 80 kPa inclusion

2.4. Directional Deformation (Y axis)

The simulation of the Y-axis deformation was conducted by applying a displacement boundary condition with a value of 0.4 mm along the positive y-axis direction. The top of the phantom was held fixed for this simulation. The corresponding images of the y-axis deformation for the 10 kPa (which is the same as the benign tissue), 40 kPa, and 80 kPa backgrounds are given in figure 5, 6, and 7.

The three images i.e. figure 5, 6, and 7 shows that the maximum y-axis deformation (0.4 mm) occurs at the bottom of the phantom, and the minimum y-axis deformation (0 mm) is at the top of the phantom.

The above observation was expected because the displacement was employed at the base, and the amount of displacement faded as it went deeper into the phantom.

2.5. Directional Deformation (X-axis)

The simulation of the X-axis deformation was conducted by applying a displacement boundary condition with a value of 0.4 mm along the positive x-axis direction. The ceiling of the phantom was held fixed for this simulation. The left and right surfaces of the phantom were free to move along the x-axis direction. The corresponding images of the x-axis deformation for the 10 kPa (which is the same as the benign tissue), 40 kPa and 80 kPa backgrounds are given in figure 8, 9, and 10.

It is seen from the figure 8, 9, and 10 that the maximum x-axis deformation occurs on both the positive and negative sides of the x-axis at the bottom of the phantom.

The above observation was expected because the displacement was employed at the base of the model, and the phantom sides were set free to shift along both directions of the x-axis.

Here, one should not be confused with the different colors of the maximum values. The colors were different because, in one direction, the displacement was the positive maximum, and in the other direction, it was the negative maximum. It can be observed from the sketching of the phantom.

2.6. Total Deformation

The total deformation is the combined deformation considering both the lateral and axial deformations of the phantom.

It can be clearly observed from the above images that the total deformations for all the phantoms with consecutive inclusions of 10 kPa, 40 kPa and 80 kPa are maximal at the bottom of the phantom. This result was expected because the maximum deformations of both phantoms were at the bottom of the phantom.

3. Simulation of the Ultrasound Signal

The ante- and post-compression RF signals can be measured utilizing the ultrasound simulation software FIELD II [36]. A typical field simulation is as follows:

- Define transducer type and create transducer
- Define the electromechanical impulse response
- Define the excitation signal
- Set initial scatterer and beam positions
- Calculate the echo signal
- Move the beam and/or scatterers to the next position and repeat

By following the above field calculation procedure, we can generate the RF signal for both the ante- and post-compression data exported from the FEM simulation. To get the RF echo signal, the following parameters were set in the FIELD II simulator:

Table 1. Transducer model parameters used to find the rf echo signal

Parameter	Value	Unit
Speed of Sound	1540	m/s
Transmitter's center frequency	3	MHz
Element's width	0.513	mm
Element's height	0.005	mm
Element number	128	No units
No. of active elements	64	No units
Sampling rate	100	MHz
Transducer Kerf	0.05	mm
Phantom area	20*20	mm ²

3.1. Ultrasound RF Signal Generation

A two-dimensional ultrasound brightness mode (B-mode) image can be obtained using the FIELD II ultrasound simulation program that displays bright dots indicating the ultrasound pulse-echo signals of tissues with different reflection properties. The brightness of each dot represents the value of the reflected echo signal. This method may grant different quantification and visualization of different structures related to anatomy, as well as for the visualization of therapeutic and diagnostic procedures for the studies of small animals.

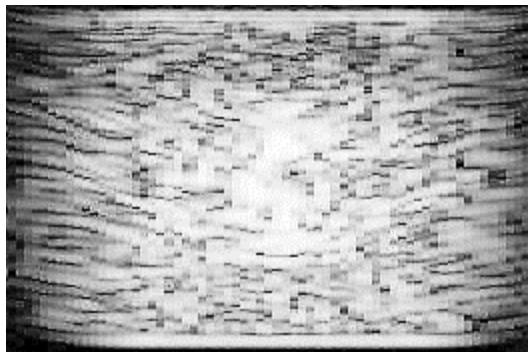


Fig. 14 Brightness mode picture of a pre-compressed phantom containing the same background and inclusion properties

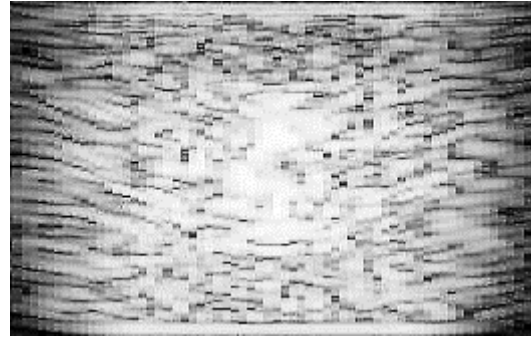


Fig. 15 Brightness mode picture of the post-compressed phantom containing the same background and inclusion properties

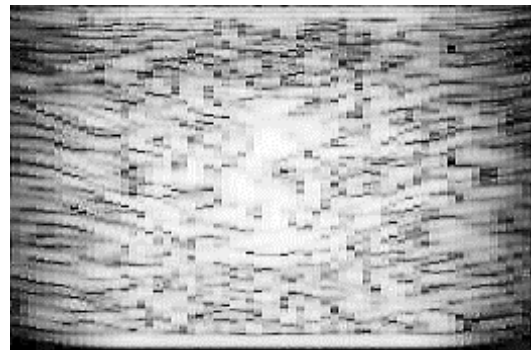


Fig. 16 Brightness mode picture of the pre-compressed phantom containing an inclusion of 40 kPa

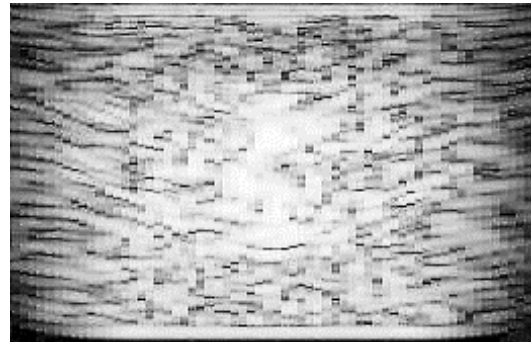


Fig. 17 Brightness mode picture of the post-compressed phantom containing an inclusion of 40 kPa

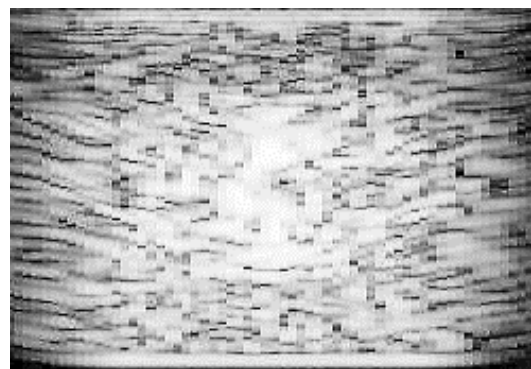


Fig. 18 Brightness mode picture of the pre-compressed phantom containing an inclusion of 80 kPa

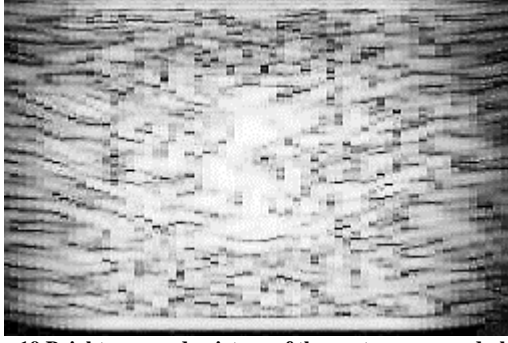


Fig. 19 Brightness mode picture of the post-compressed phantom containing an inclusion of 80 kPa

4. Results and Discussion

The major aim of this article is to propose an imaging technique that introduces a new time delay estimation algorithm and reduces the computational cost of elastography. To perform this task, as mentioned above, a 20mm×20mm square phantom is constructed with 2000 randomly located scatterers; this phantom includes a circular shape with a radius of 10mm. After that, for a given movement (which is 2% of the model height), the model was simulated using ANSYS software for the FEM. To clarify the effectiveness of the proposed method, the phantom was run for different Young’s moduli both for the background and for inclusion. An ultrasound simulation program named FIELD II was used for the ultrasound simulation. The program has superb modeling of transducer features along with good wave focusing, interactions and beam focusing. A linear array transducer probe containing a center frequency of 3.5 MHz and a sampling rate of 100 MHz was modeled in FIELD II.

For the simulation, a linear array-type transducer was modeled and used, which has a 100 MHz sample frequency and a 3.5 MHz center frequency. The chosen transducer had 64 active transducers along with 128 radiofrequency (RF) lines. In this article, a time delay measurement method which is a 2D cross-correlation function, is utilized that provides the cross-correlation of ante- and post-compression RF echoes. One of the major disadvantages of direct strain imaging is the computational cost. To overcome this problem, the strain estimation step was skipped, and the MATLAB tool name surf was introduced to map the attained correlated delay values. The surf image shows that the scatterers are less displaced and that the scatterers are more displaced. The conventional strain imaging technique and the proposed technique are discussed below.

4.1. Conventional Strain Imaging Technique

The strain imaging technique has earned importance in recent years for diagnosing cancers or tumors. In this technique, an ultrasound probe is used to deform tissue across the region of interest by applying mechanical compression because of the different tissue stiffness properties various displacements of tissue result in various time shifts in the achieved RF signals. The successive ultrasound RF echoes were achieved before and after compression of the phantom. Then, a time delay estimation algorithm is utilized to calculate the displacement among ante- and post-compression RF signals. Then the local tissue delays are measured from the above time delays whose axial gradient gives the estimated strain [33]. The flow chart for estimating the strain and imaging results is given below.

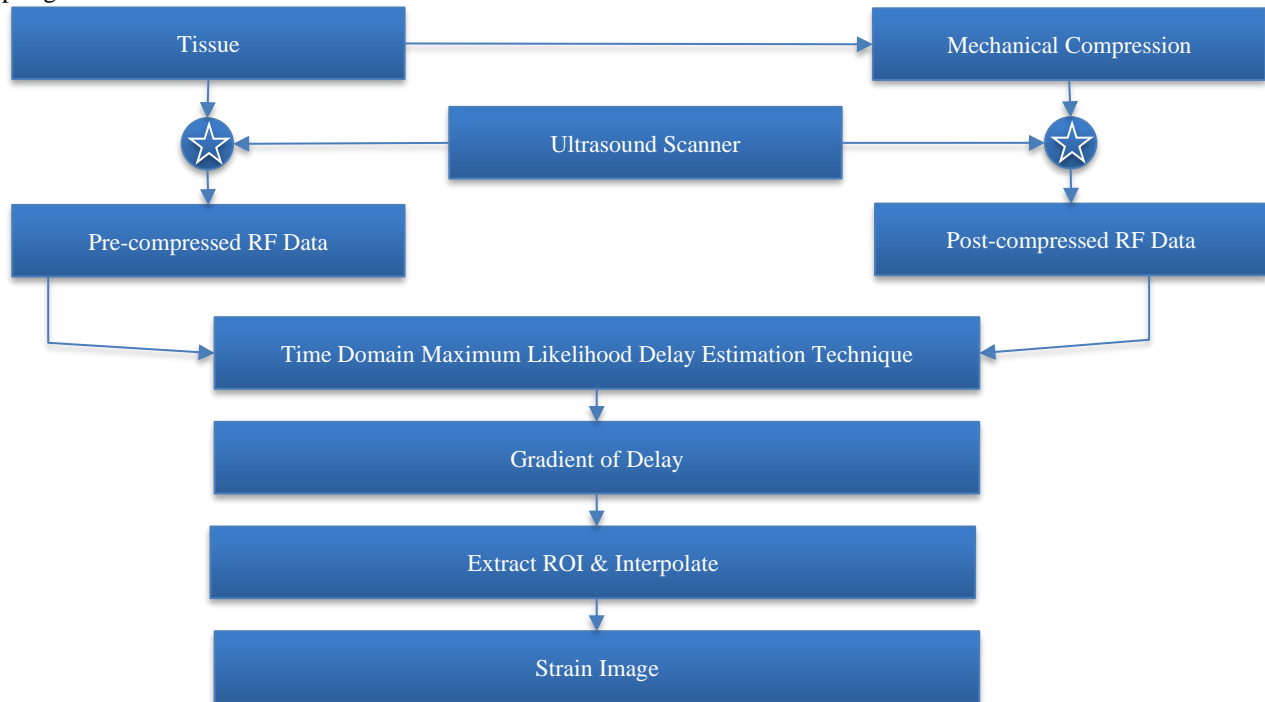


Fig. 20 Flow chart for conventional strain imaging technique

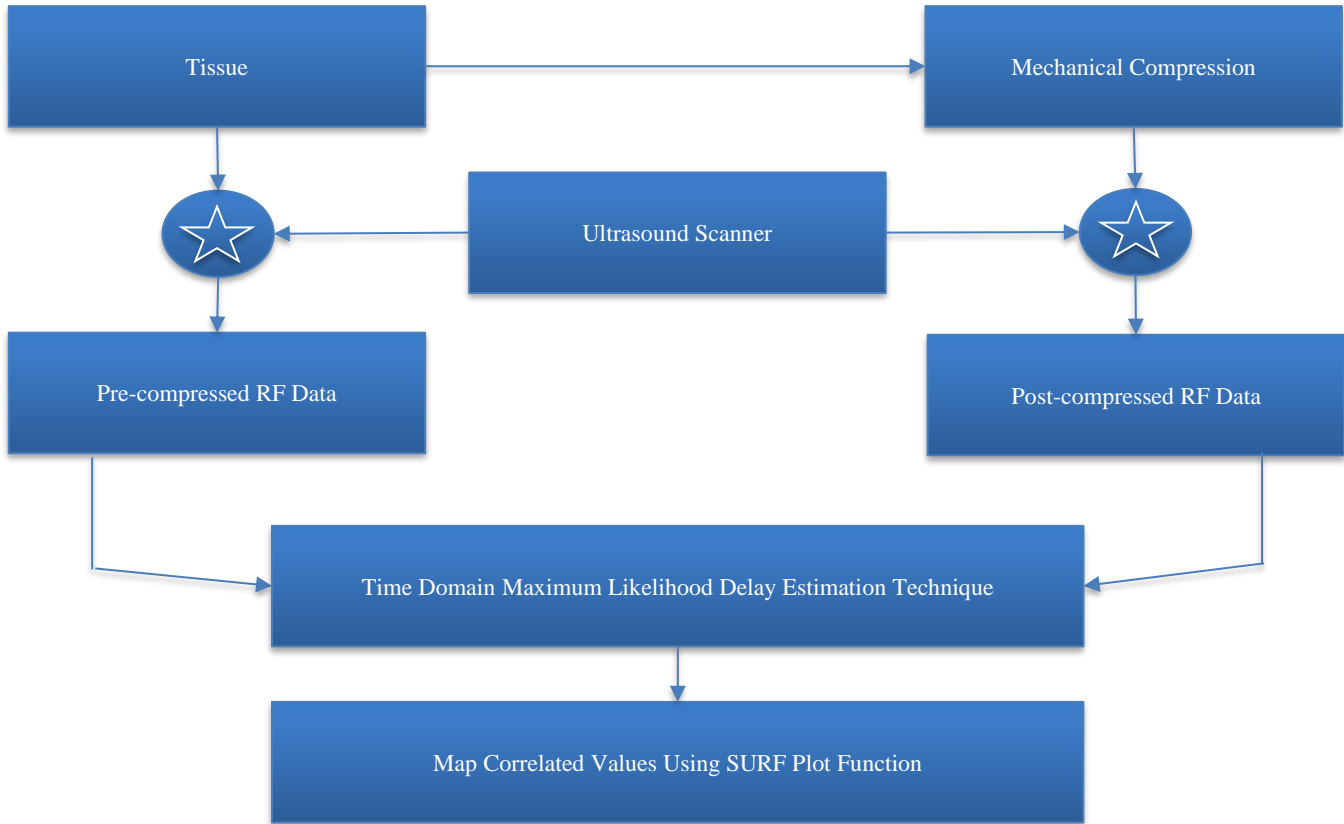


Fig. 21 Flowchart of the proposed method for obtaining ultrasound images

4.2. Proposed Ultrasound Imaging Technique

As mentioned earlier, the main purpose of this paper is to introduce a new time delay estimation technique and to design an algorithm that is less computationally costly than estimating strain. To do this, we follow the same conventional workflow except for the use of a 2D cross-correlation technique for estimating the time delay and the use of the MATLAB surf tool to visualize the correlation between the pre- and post-compression RF data. The flowchart of the proposed imaging technique is given above.

4.3. Extraction of Correlated Values using 2D cross-Correlation

Correlation is an operation that is used to measure the degree of similarity between two signals to extract information that depends largely on the application. The correlation technique is a widely used approach for estimating the delay between two signals. In that case, it can be utilized to estimate the displacement between pre- and post-compressed signals. To accomplish this task, a two-dimensional delay estimation function named `xcorr2` is used. The command `xcorr2(X, Y)` of MATLAB gives us the correlation matrix in two-dimensional form.

4.4. Mapping of Correlated Values

In this paper, an imaging technique that is less computationally is developed from ante- and post-

compression RF signals. To reduce the computational cost of the proposed method, rather than direct strain estimation using correlated values, the surf tool was used to visualize the correlated values. In the simulated images, we can see where the individual RF signals are better matched (less displaced) and where they are less matched (more displaced.). The mapping of correlated values for different inclusion properties is given in the following Figures 22, 23, and 24.

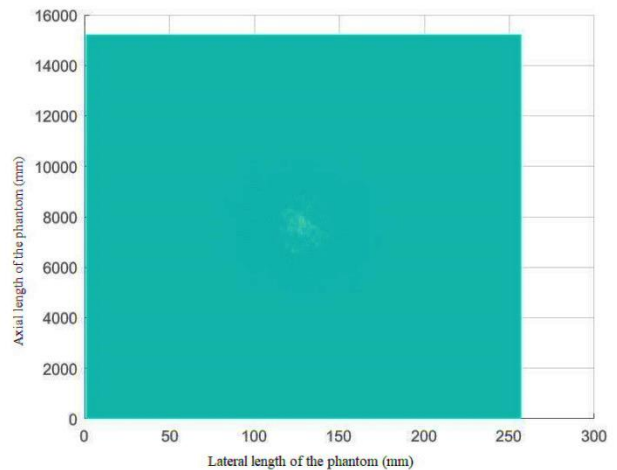


Fig. 22 Mapping of correlation values achieved from pre- and post-compression phantom when the inclusion (10 kPa) is the same as the background (10 kPa)

Figure 22 shows the mapping of correlated RF echo signal values obtained from pre- and post-compression phantoms when the hardness of inclusion of the phantom is the same as that of the background of the phantom. As Young’s moduli for both the inclusion and the background are the same, the displacement of the scatterers decreases as the depth of the phantom increases.

Therefore, the maximum number of scatterers displaced from the original location indicates that a small number of scatterers yield the best matching results. Therefore, it can be observed from the above image that the inclusion is not clearly distinguishable from the background. This means that there may be no differentiable malignant tissue in the phantom. Theoretically, the inclusion and background should not be 100% distinguishable. But due to rounding off the received RF data some data are lost, which results in slight noise.

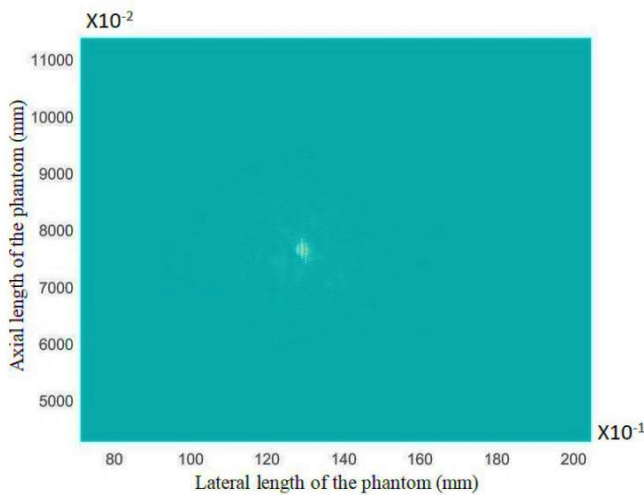


Fig. 23 Mapping of correlation values achieved from pre- and post-compression phantom when the inclusion (40 kPa) is 4 times stronger than the background (10 kPa).

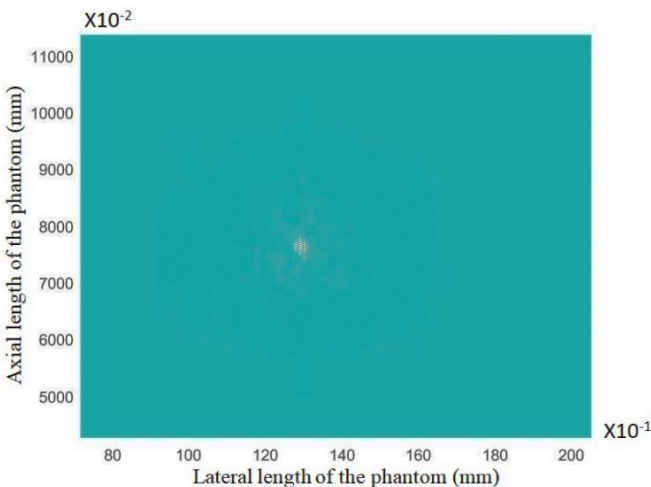


Fig. 24 Mapping of correlation values achieved from pre- and post-compression phantom when the inclusion (80 kPa) is 8 times harder than the background (10 kPa)

The figure 23 shows the mapping of correlated RF echo signals obtained from pre- and post-compression phantom images when the hardness of the inclusion of the phantom was 4 times stronger than that of the background. As the inclusion’s Young’s modulus is 4 times stronger than that of the background, the displacement of the scatterers after compression is less for the inclusion than for the background of the phantom.

The figure 24 shows the mapping of correlated RF echo signals obtained from pre- and post-compression phantom images when the hardness of the inclusion of the phantom is 8 times harder than that of the background. As Young’s modulus of the inclusion is 8 times larger than that of the background, the displacement of the scatterers after compression is less for the inclusion than for the background of the phantom. Therefore, when it is taken the correlated values of the pre- and post-compression RF echo signals using the xcorr2 MATLAB function the scatterers of the inclusion show the best matching results. For that reason, it can be observed from the above image that the inclusion is distinguishable from the background. This means that there may be different malignant tissue in the phantom located at the center of the phantom.

5. Comparison

5.1. Comparison between Conventional Strain Imaging and the Proposed Method

Figure 25 shows the FEM model of the phantom for the conventional strain imaging technique. In this figure, the malignant tissue is shown in the middle of the phantom. The aim was to evaluate strain imaging from which malignant tissue might be detected. The strain image of a given phantom is shown in Figure 26, where the strain is estimated using a typical one-dimensional cross-correlation algorithm. The given image is a brightness mode (B-mode) image and from this image, we can detect different objects that are different from their surroundings (objects encircled by yellow circles). However, it was expected that only one object would be found near the center of the phantom; it can be assumed that the large yellow circle encircles this object. However, other objects can also be detected in the image (encircled by the small yellow circle). Therefore, it is difficult to choose which tissue is the actual malignant tissue, and whether there is more than one malignant tissue in the phantom is unclear.

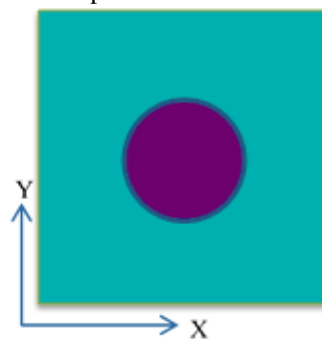


Fig. 25 FEM model of the phantom for conventional strain imaging

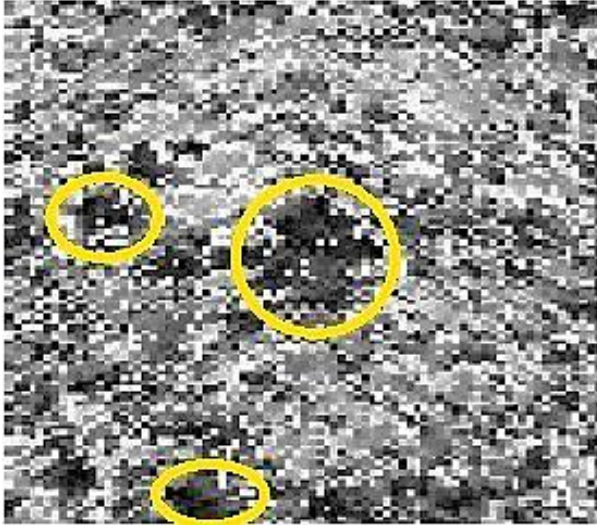


Fig. 26 Strain image achieved from traditional cross-correlation without interpolation

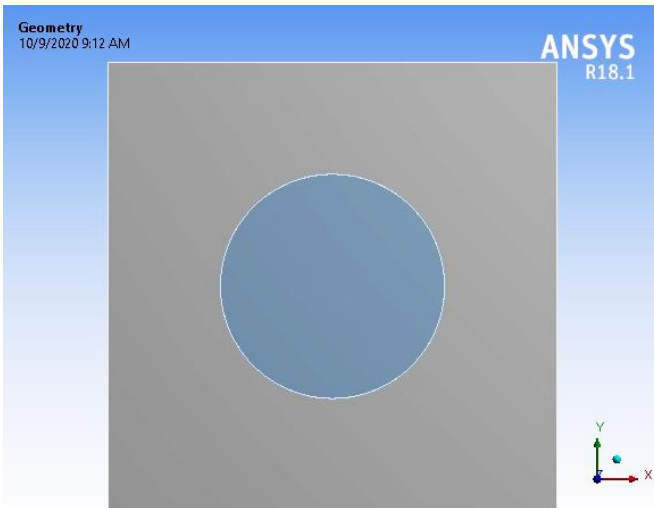


Fig. 27 FEM model of the phantom for imaging using the proposed method

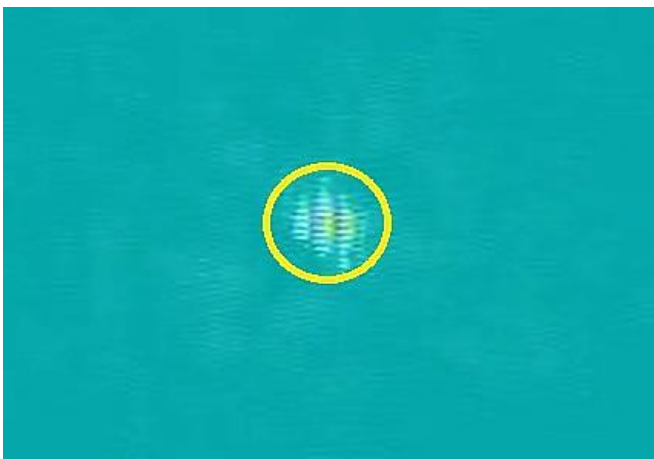


Fig. 28 Mapping of correlated values when the Young's modulus of the inclusion is 4 times larger than the Young's modulus of the background

The above figure shows the FEM model of the phantom for the proposed method. In this figure, it can be seen that the malignant tissue is located directly in the middle of the phantom, which is similar to Figure 25. The aim was to run the phantom, figure out the correlated values, and map them.

The above image was obtained from the mapping of correlated values using the MATLAB surf tool, where 2-D cross-correlation was used to estimate the delay. The given image is a brightness mode (B-mode) image.

From this image, an object can be detected that is different from its surroundings (objects encircled by the yellow circles), as was expected, because there was only one circular malignant tissue right at the center of the phantom, which was not in the case of strain imaging. Therefore, it seems that there is no ambiguity in finding only malignant tissue. Therefore, the proposed method performed better than the conventional strain imaging technique in detecting abnormalities in tissue.

5.2. Quantitative Comparison between Conventional Strain Imaging and the Proposed Method

However, 2D time delay estimation is better than 1D time delay estimation [9]. Here, the correlation between the conventional and proposed methods using 2D delay estimation is analyzed.

To correlate the suggested method with conventional strain imaging methods quantitatively, the elapsed time of each step is calculated using the MATLAB tic toc function. As we already know, all imaging has pre-imaging and post-imaging processes. Therefore, the analysis of the comparison breaks down into two parts.

Based on the above- procedure, the calculated pre-imaging elapsed time (only the pre- and post-compression elapsed time) using 1D time delay estimation exceeded the whole simulation elapsed time of the proposed method. Therefore, for a fair comparison, the elapsed time of 2D-time delay estimation is calculated for both methods. The table of the estimated elapsed time for different simulations is given below:

Table 2. Estimated elapsed time for different simulations

Simulations	Time Elapsed
1D pre-compression	95.6088099 seconds
1D post compression	142.494453 seconds
2D pre-compression	96.143224 seconds
2D post compression	94.307406 seconds
2D cross-correlation	31.574962 seconds
2D surf Mapping	0.046730 seconds
Gradient of delay	0.067423 seconds

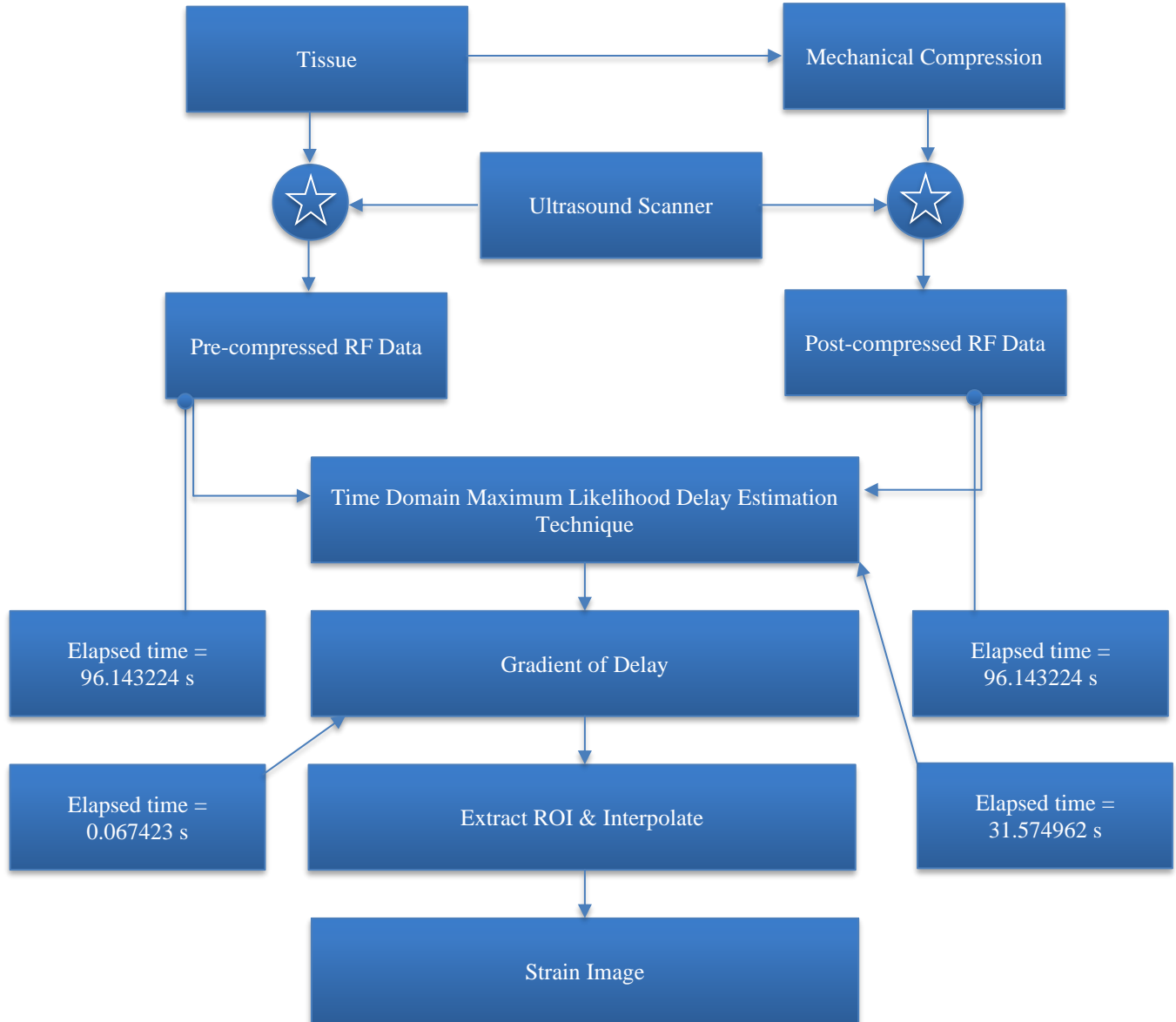


Fig. 29 Flow chart for estimating the strain and imaging using conventional technique with elapsed time

Now, to compare the methods, a flow chart is constructed for both methods, where each step contains its elapsed time. To make the comparison more meaningful, first, the elapsed times in the equations were written.

Let's assume that the total time required for the execution of conventional strain imaging is-

$$Y = S_{pre} + S_{post} + T_{DS} + G_{DS} + E_s + S_s \quad (1)$$

Where,

Y = the total elapsed time for the execution of the conventional strain imaging.

S_{pre} = elapsed time for pre-compression ultrasound simulation of the strain imaging.

S_{post} = elapsed time for post-compression ultrasound

simulation of the strain imaging.

T_{DS} = elapsed time to find the delay time among ante- and post-compression RF signals for strain imaging.

G_{DS} = elapsed time to calculate delay gradient.

E_s = elapsed time to estimate the strain.

S_s = elapsed time to perform strain imaging.

Here, $(S_{pre} + S_{post} + T_{DS})$, is the pre-processing time of the imaging.

The total time needed for this preprocessing time-

$$S_{pre} + S_{post} + T_{DS} = 96.143224 + 94.307406 + 31.574962 = 222.025592 \text{ seconds}$$

Additionally, in the post-process imaging, G_{DS} = 0.067423 second.

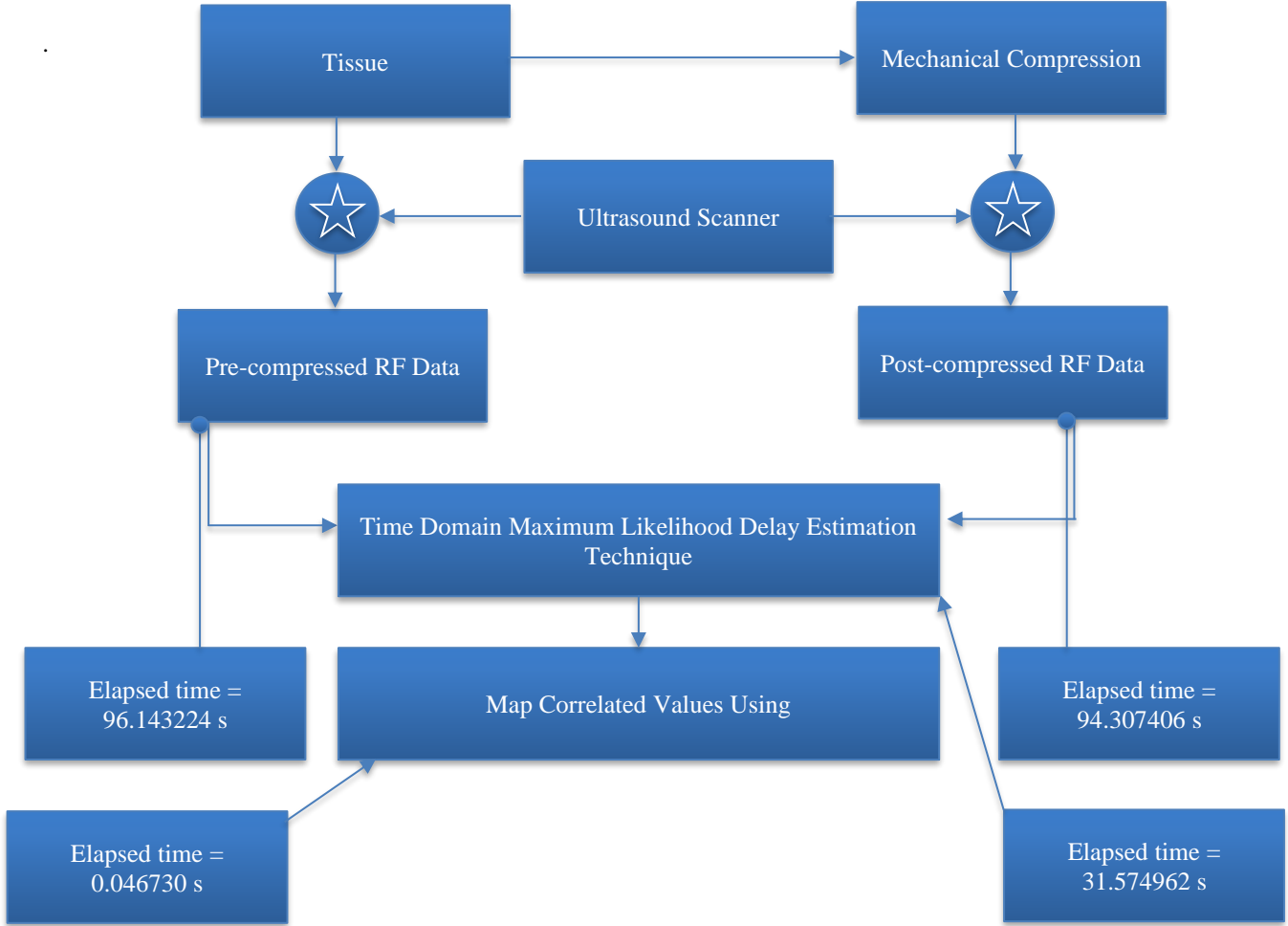


Fig. 30 Ultrasound imaging flow chart utilizing the proposed method with elapsed time

Now, by examining the flow chart of the proposed method, another equation can be written for the proposed method.

$$X = C_{pre} + C_{post} + T_{DC} + M_c \quad (2)$$

Where,

X = total elapsed time for the execution of the proposed method.

C_{pre} = elapsed time for pre-compression ultrasound simulation of the proposed method.

C_{post} = elapsed time for post-compression ultrasound simulation of the proposed method.

T_{DC} = elapsed time to find the delay time among ante- and post-compression RF signals for the suggested method.

M_c = elapsed time for mapping the correlated values.

Here, $(C_{pre} + C_{post} + T_{DC})$, is the pre-processing time of the imaging.

The total time needed for this pre-process-
 $C_{pre} + C_{post} + T_{DC} = 96.143224 + 94.307406 + 31.574962 =$

222.025592 seconds.

In the post-process imaging, $M_c = 0.046730$ seconds. Therefore, from the above information, it can be said that the total imaging time needed for the execution of the proposed method, $X = 222.025592 + 0.046730$ seconds and the total time needed for the execution of conventional strain imaging are

$$Y = 222.025592 + 0.067423 + E_s + S_s \quad (3)$$

Now, in Y , the pre-process time and G_{DS} cumulatively exceeded the elapsed time for the whole execution of the proposed method.

Additionally, $(E_s + S_s)$ is a non-zero and non-negative required time that is not even needed to calculate for comparison. Because by excluding these two elapsed times, it is seen that, Y requires more time than X for execution. Therefore, considering the above discussion, it can be said that the proposed method is less computationally costly than the conventional strain imaging method.

6. Conclusion

In this paper, the 2D tissue displacement of the phantom (both horizontal and vertical) model was measured. The displacements and the (x, y) coordinates were exported from the ANSYS design modeler. Then, the ante- and post-compression (x, y) coordinates were measured. To obtain the ultrasound RF signal, FIELD II simulation software was used to find the pre- and post-compression RF signals. The 2D MATLAB function named `xcorr2` is utilized to figure out the displacement among the ante- and post-compression RF

signals. The acquired signal is basically attained using the sample tracking method rather than the window-based technique. The attained cross-correlation value was mapped using the MATLAB `surf` function. The mapped image shows promising results in finding malignant tissue with an ambiguity from the phantom. To compare computational cost, the MATLAB `tic toc` function is used to measure the total simulation time. The simulation time measurements show that the proposed method requires less simulation time than does the conventional strain imaging method.

References

- [1] Jonathan Ophir et al., “Elastography: A Quantitative Method for Imaging the Elasticity of Biological Tissues,” *Ultrasonic Imaging*, vol. 13, pp. 111–134, 1991. [[CrossRef](#)] [[Google Scholar](#)] [[Publisher Link](#)]
- [2] Andreas Heimdal et al., “Real-Time Strain Rate Imaging of the Left Ventricle by Ultrasound,” *Journal of the American Society of Echocardiography*, vol. 11, no. 11, pp. 1013–1019, 1998. [[CrossRef](#)] [[Google Scholar](#)] [[Publisher Link](#)]
- [3] Laurence N. Bohs, Barry H. Friemel, and Gregg E. Trahey, “Experimental Velocity Profiles and Volumetric Flow via Two-Dimensional Speckle Tracking,” *Ultrasound in Medicine & Biology*, vol. 21, no. 7, pp. 885–898, 1995. [[CrossRef](#)] [[Google Scholar](#)] [[Publisher Link](#)]
- [4] M. Lubinski, S. Emelianov, and M. O’Donnell, “Speckle Tracking Methods for Ultrasonic Elasticity Imaging Using Short-Time Correlation,” *IEEE Transactions on Ultrasonics, Ferroelectrics, and Frequency Control*, vol. 46, no. 1, pp. 82–96, 1999. [[CrossRef](#)] [[Google Scholar](#)] [[Publisher Link](#)]
- [5] S. Srinivasan, and Jonathan Ophir, “A Zero-Crossing Strain Estimator in Elastography,” *Ultrasound in Medicine & Biology*, vol. 29, no. 2, pp. 227–238, 2003. [[CrossRef](#)] [[Google Scholar](#)] [[Publisher Link](#)]
- [6] C. Kasai et al., “Real-Time Two-Dimensional Blood Flow Imaging Using an Autocorrelation Technique,” *IEEE Transactions on Sonics and Ultrasonics*, vol. 32, no. 3, pp. 458–464, 1985. [[CrossRef](#)] [[Google Scholar](#)] [[Publisher Link](#)]
- [7] T. Loupas, R.B. Peterson, and R.W. Gill, “Experimental Evaluation of Velocity and Power Estimation for Ultrasound Blood Flow Imaging, by Means of a Two-Dimensional Autocorrelation Approach,” *IEEE Transactions on Ultrasonics, Ferroelectrics, and Frequency Control*, vol. 42, no. 4, pp. 689–699, 1995. [[CrossRef](#)] [[Google Scholar](#)] [[Publisher Link](#)]
- [8] H. Torp, K. Kristoffersen, and B.A.J. Angelsen, “Autocorrelation Techniques in Color Flow Imaging: Signal Model and Statistical Properties of the Autocorrelation Estimates,” *IEEE Transactions on Ultrasonics, Ferroelectrics, and Frequency Control*, vol. 41, no. 5, pp. 604–612, 1994. [[CrossRef](#)] [[Google Scholar](#)] [[Publisher Link](#)]
- [9] F. Viola, and W.F. Walker, “A Comparison of the Performance of Time-Delay Estimators in Medical Ultrasound,” *IEEE Transactions on Ultrasonics, Ferroelectrics, and Frequency Control*, vol. 50, no. 4, pp. 392–401, 2003. [[CrossRef](#)] [[Google Scholar](#)] [[Publisher Link](#)]
- [10] G.F. Pinton, J.J. Dahl, and G.E. Trahey, “Rapid Tracking of Small Displacements with Ultrasound,” *IEEE Transactions on Ultrasonics, Ferroelectrics, and Frequency Control*, vol. 53, no. 6, pp. 1103–1117, 2006. [[CrossRef](#)] [[Google Scholar](#)] [[Publisher Link](#)]
- [11] I.A. Hein, and W.D. O’Brien, “Current Time-Domain Methods for Assessing Tissue Motion by Analysis from Reflected Ultrasound Echoes—A Review,” *IEEE Transactions on Ultrasonics, Ferroelectrics, and Frequency Control*, vol. 40, no. 2, pp. 84–102, 1993. [[CrossRef](#)] [[Google Scholar](#)] [[Publisher Link](#)]
- [12] Gianmarco F. Pinton, and Gregg E. Trahey, “Continuous Delay Estimation with Polynomial Splines,” *IEEE Transactions on Ultrasonics, Ferroelectrics, and Frequency Control*, vol. 53, no. 11, pp. 2026–2035, 2006. [[CrossRef](#)] [[Google Scholar](#)] [[Publisher Link](#)]
- [13] G. Jacovitti, and G. Scarano, “Discrete Time Techniques for Time Delay Estimation,” *IEEE Transactions on Signal Processing*, vol. 41, no. 2, pp. 525–533, 1993. [[CrossRef](#)] [[Google Scholar](#)] [[Publisher Link](#)]
- [14] S. Langeland et al., “A Simulation Study on the Performance of Different Estimators for Two-Dimensional Velocity Estimation,” *2002 IEEE Ultrasonics Symposium, Proceedings*, Munich, Germany, vol. 2, pp. 1859–1862, 2002. [[CrossRef](#)] [[Google Scholar](#)] [[Publisher Link](#)]
- [15] M.B. Hisham et al., “Template Matching Using Sum of Squared Difference and Normalized Cross Correlation,” *2015 IEEE Student Conference on Research and Development (SCOReD)*, Kuala Lumpur, Malaysia, pp. 100-104, 2015. [[CrossRef](#)] [[Google Scholar](#)] [[Publisher Link](#)]
- [16] Hiroaki Niitsuma, and Tsutomu Maruyama, “Sum of Absolute Difference Implementations for Image Processing on FPGAs,” *2010 International Conference on Field Programmable Logic and Applications*, Milan, Italy, pp. 167-170, 2010. [[CrossRef](#)] [[Google Scholar](#)] [[Publisher Link](#)]
- [17] Anton Fertner, and Anders Sjolund, “Comparison of Various Time Delay Estimation Methods by Computer Simulation,” *IEEE Transactions on Acoustics, Speech, and Signal Processing*, vol. 34, no. 5, pp. 1329-1330, 1986. [[CrossRef](#)] [[Google Scholar](#)] [[Publisher Link](#)]

- [18] Isaac N. Bankman, *Handbook of Medical Image Processing and Analysis*, 2nd ed., Academic Press, Elsevier Science, Pages 435-452, 2009. [[Google Scholar](#)] [[Publisher Link](#)]
- [19] T. Varghese et al., “Tradeoffs in Elastographic Imaging,” *Ultrasonic Imaging*, vol. 23, no. 4, pp. 216–248, 2001. [[CrossRef](#)] [[Google Scholar](#)] [[Publisher Link](#)]
- [20] Hairong Shi, and Tomy Varghese, “Two-Dimensional Multi-Level Strain Estimation for Discontinuous Tissue,” *Physics in Medicine & Biology*, vol. 52, no. 2, pp. 389–401, 2007. [[CrossRef](#)] [[Google Scholar](#)] [[Publisher Link](#)]
- [21] C. Sumi, “Fine Elasticity Imaging Utilizing the Iterative RF-echo Phase Matching Method,” *IEEE Transactions on Ultrasonics, Ferroelectrics, and Frequency Control*, vol. 46, no. 1, pp. 158–166, 1999. [[CrossRef](#)] [[Google Scholar](#)] [[Publisher Link](#)]
- [22] Reza Zahiri-Azar, and Septimiu E. Salcudean, “Time-Delay Estimation in Ultrasound Echo Signals Using Individual Sample Tracking,” *IEEE Transactions on Ultrasonics, Ferroelectrics, and Frequency Control*, vol. 55, no. 12, pp. 2640-2650, 2008. [[CrossRef](#)] [[Google Scholar](#)] [[Publisher Link](#)]
- [23] Jonathan Ophir et al., “Elastography: Ultrasonic Imaging of Tissue Strain and Elastic Modulus in Vivo,” *European Journal of Ultrasound*, vol. 3, no. 1, pp. 49–70, 1996. [[CrossRef](#)] [[Google Scholar](#)] [[Publisher Link](#)]
- [24] E.I. Céspedes et al., “Elastography: Elasticity Imaging Using Ultrasound with Application to Muscle and Breast in Vivo,” *Ultrasonic Imaging*, vol. 15, no. 2, pp. 73–88, 1993. [[CrossRef](#)] [[Google Scholar](#)] [[Publisher Link](#)]
- [25] Jonathan Ophir et al., “Elastography: Imaging the Elastic Properties of Soft Tissues with Ultrasound,” *Journal of Medical Ultrasonics*, vol. 29, pp. 155–171, 2002. [[CrossRef](#)] [[Google Scholar](#)] [[Publisher Link](#)]
- [26] R. Zahiri-Azar, and S.E. Salcudean, “Motion Estimation in Ultrasound Images Using Time Domain Cross Correlation with Prior Estimates,” *IEEE Transactions on Biomedical Engineering*, vol. 53, no. 10, pp. 1990–2000, 2006. [[CrossRef](#)] [[Google Scholar](#)] [[Publisher Link](#)]
- [27] S. Kaisar Alam, “Novel Spline-Based Approach for Robust Strain Estimation in Elastography,” *Ultrasonic Imaging*, vol. 32, no. 2, pp. 91–102, 2010. [[CrossRef](#)] [[Google Scholar](#)] [[Publisher Link](#)]
- [28] S. Kaisar Alam, Jonathan Ophir, and E.E. Konofagou, “An Adaptive Strainestimator for Elastography,” *IEEE Transactions on Ultrasonics, Ferroelectrics, and Frequency Control*, vol. 45, no. 2, pp. 461–472, 1998. [[CrossRef](#)] [[Google Scholar](#)] [[Publisher Link](#)]
- [29] S. Kaisar Alam et al., “Elastography: Ultrasonic Estimation and Imaging of the Elastic Properties of Tissues,” *Proceedings of the Institution of Mechanical Engineers, Part H: Journal of Engineering in Medicine*, vol. 213, no. 3, pp. 203–233, 1999. [[CrossRef](#)] [[Google Scholar](#)] [[Publisher Link](#)]
- [30] Mohammad Arafat Hussain et al., “Direct and Gradient-Based Average Strain Estimation by Using Weighted Nearest Neighbor Cross-Correlation Peaks,” *IEEE Transactions on Ultrasonics, Ferroelectrics, and Frequency Control*, vol. 59, no. 8, pp. 1713-1728, 2012. [[CrossRef](#)] [[Google Scholar](#)] [[Publisher Link](#)]
- [31] T. Varghese et al., “Direct Strain Estimation in Elastography Using Spectral Cross-Correlation,” *Ultrasound in Medicine & Biology*, vol. 26, no. 9, pp. 1525–1537, 2000. [[CrossRef](#)] [[Google Scholar](#)] [[Publisher Link](#)]
- [32] S. Kaisar Alam et al., “Adaptive Spectral Strain Estimators for Elastography,” *Ultrasonic Imaging*, vol. 26, no. 3, pp. 131–149, 2004. [[CrossRef](#)] [[Google Scholar](#)] [[Publisher Link](#)]
- [33] Md. Maruf Hossain Shuvo, A.B.M. Aowlad Hossain, and Krishna Chandra Roy, “Ultrasound Strain Imaging Based on Information Theoretic Delay Estimation,” *2014 17th International Conference on Computer and Information Technology (ICCI)*, Dhaka, Bangladesh, pp. 401-405, 2014. [[CrossRef](#)] [[Google Scholar](#)] [[Publisher Link](#)]
- [34] Gérard Blanchet, and Maurice Charbit, *Digital Signal and Image Processing Using MATLAB*, Wiley-ISTE, 2006. [[Publisher Link](#)]
- [35] Rafael C. Gonzalez, Richard E. Woods, and Steven L. Eddins, *Digital Image Processing Using MATLAB*, Gatesmark Publishing, 2020. [[Publisher Link](#)]
- [36] Jorgen Arendt Jensen, “Field: A Program for Simulating Ultrasound Systems,” *10th Nordic-Baltic Conference on Biomedical Imaging, Published in Medical & Biological Engineering & Computing*, vol. 34, pp. 351-353, 1996. [[Google Scholar](#)] [[Publisher Link](#)]
- [37] Sen Zhong, Wei Xia, and Zishu He, “Approximate Maximum Likelihood Time Differences Estimation in the Presence of Frequency and Phase Consistence Errors,” *IEEE International Symposium on Signal Processing and Information Technology*, Athens, Greece, pp. 305-308, 2013. [[CrossRef](#)] [[Google Scholar](#)] [[Publisher Link](#)]